



Effects of Feeding Mode and Inlet Area Ratio on Heating Characteristics in Dual-Inlet Swirl Tubes

X. Xu¹, J. Wang¹, Q. Yang^{2†}, H. Liu² and H. Wang²

¹ School of Mechanical and Power Engineering, East China University of Science and Technology, Shanghai 200237, P. R. China

² State Key Laboratory of Chemical Engineering, East China University of Science and Technology, Shanghai 200237, P. R. China

†Corresponding Author Email: qyang@ecust.edu.cn

(Received April 30, 2020; accepted October 31, 2020)

ABSTRACT

A preheating exchanger is developed for improving acidic water degassing. Reasonable optimization of dual-inlet swirl heating tubes is analyzed by computations of the flow and heat transfer. The comparisons of the swirl number and circumferential average Nusselt number between isobaric injection and isokinetic injection are performed. Inlet area ratios ranging from 0.1 to 0.9 exhibit an important influence on the flow phenomena and the heating performance. A lower value of inlet area ratio leads to the tendency for the fluid passing through inlet 2 to move upstream of inlet 2 and results in more vortex pairs between inlets 1 and 2. An inlet area ratio value of 0.5 exhibits the largest global average Nusselt number, normalized Nusselt number, and thermal performance factor. The optimized inlet area ratio is suitable for improving the degassing efficiency.

Keywords: Preheating degassing; Dual-inlet swirl; Flow and heat transfer; Numerical simulations.

1. INTRODUCTION

In recent years, dual-inlet swirl tubes have been developed for hydrocarbon stripping from acidic water by coupling with degassing cyclone separators. A dual-inlet swirl tube is commonly used to preheat acidic water and to improve the degassing efficiency. A typical process flow of acidic water degassing is shown in Fig. 1. Acidic water is produced in the fractionator top when the temperature is lower than the dew point. Then, the acidic water is cooled into a settler to remove the oil phase. Next, the reservoir is operated under a pressure of 0.2 MPa and a temperature of 25 °C to separate most of the hydrocarbons. However, the residual hydrocarbons in the acidic water lead to abnormal parameters for the stripper. For example, if hydrocarbons flow into the stripper, gaseous hydrocarbons are enriched at the top of the stripper tower. Then, the pressure and temperature at the top of the stripper tower rise sharply, leading to an unstable liquid level. As a result, a preheating system is essentially needed for degassing cyclones.

Degassing cyclones have been discussed before (Xu *et al.* 2016, Xu *et al.* 2015). The pressure gradient, the centrifugal force acting on the gas-liquid interface, and the combination strategy of cyclones

have been illustrated in the literature (Xu *et al.* 2018, Xu *et al.* 2019). To further improve the degassing efficiency, preheating before the degassing cyclone is a feasible solution. As illustrated by Biegger (Biegger *et al.* 2018), if one is interested in the maximum heat transfer caused by a high pressure loss, a swirl tube with one inlet is the best choice. If a lower but more homogeneous heat transfer with a lower pressure loss is desired, one should choose a swirl tube with multiple inlets. Here, we develop a preheating swirl tube with dual inlets and a degassing cyclone for removing residual hydrocarbons in acidic water. Optimization of the heating characteristics in the dual-inlet swirl tube has an important influence on the hydrocarbon removal from acidic water.

Enhancing exchanger performance can produce more economical designs of heat exchangers, which can aid in producing energy, material and cost savings related to a heat exchange process (Awais and Bhuiyan 2018). Swirl flow devices have been widely used for increasing convective heat transfer in various industries (Hong *et al.* 2018). For example, the tangential cyclone heat exchanger is used for the for effective heat exchange between two medium (Mothilal *et al.* 2018). Kreith and Margolis suggested that surface heat transfer could

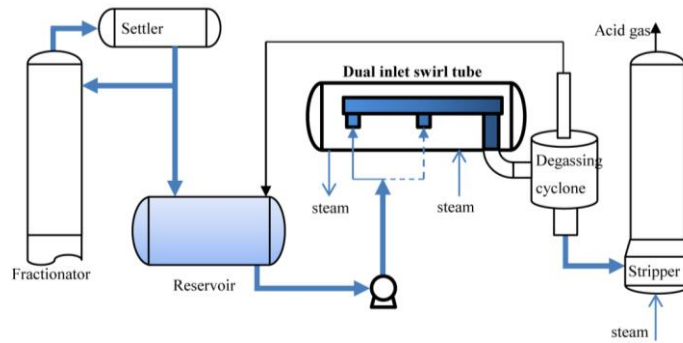


Fig. 1. A typical process flow of acidic water degassing in which the dual-inlet swirl tube is used to preheat the acidic water.

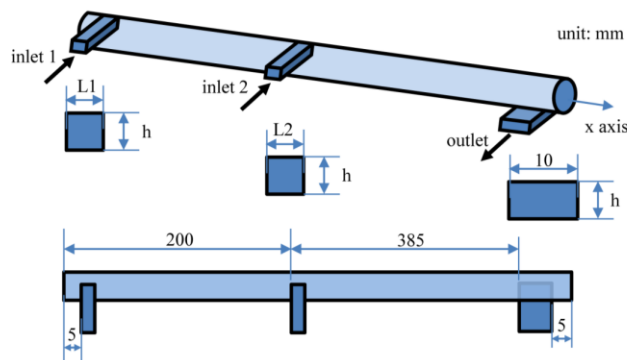


Fig. 2. Structure of the dual-inlet swirl tube.

be enhanced by introducing jets tangentially into a tube at various locations to generate vortex flow (Kreith and Margolis 1959). One of the schemes for inducing vortex flow is to use tangential injection holes. Swirl flow also forms resulting from other kinds of inducers, such as swirl vanes or curved rods (Sheikholeslami *et al.* 2015). The inlet locations play an influence on the heat transfer rate and the temperature uniformity (Khaleghinia *et al.* 2019). The vortex motion can be maintained by repeated addition of fluid through appropriately spaced injection holes for any desired distance. For manufacturing convenience, the holes are commonly simplified as inlet slots located at the beginning and middle sections of the swirl chamber (Ling *et al.* 2006). The swirl flow induced by wire coil provides a more effective overall heat transfer efficiency compared to the non-swirl flow by rings insert which exhibits the potential advantages of the swirl heating tube (Vahidifar and Kahrom 2015).

In this work, tangential inlets are located at the beginning and middle sections of the swirl chamber. The outlet is located at the end sections of the swirl chamber. A deadman length of 5 mm for actual installation is kept at both ends of the chamber.

A large number of studies on swirling flow characteristics have been conducted in which experimental and numerical results have provided suitable and reasonable data (Chen *et al.* 2019, Jafari *et al.* 2017). This paper presents a numerical study of the heat transfer and hydrodynamic characteristics in dual-inlet swirl tubes. The fluid

dynamics and heat transfer of swirling decaying flow for heating water are cited from the literature (Chen *et al.* 2016a). The computations of the flow and heat transfer in the swirl tubes are performed using the commercial software ANSYS CFX, which has been used in the literature (Chen *et al.* 2016b). To investigate the impacts of inlet chamber configurations on a swirl chamber, this paper introduces two different configurations of inlet chambers. When the two inlets have equal areas, isobaric injection and isokinetic injection are contrastively studied. When the two injection inlets have different areas, the effect of the ratio of the two inlet areas on heat transfer is verified. The injection configurations are improved in this work, which will be beneficial for the industrial application of heat transfer swirl tubes.

2. NUMERICAL SETUP

2.1 Geometrical Details

A 400-mm-long circular tube with a diameter of 20 mm is used as the main heating tube. The heating process occurs at the tube surface. The dual-inlet swirl tube has two tangential inlets and one tangential outlet, named inlet 1, inlet 2, and outlet, respectively. The sum of the inlet area, which is the sum of the areas of inlets 1 and 2, is equal to that of the outlet and remains constant. The heights of the inlets and outlet have the same value, $h = 5$ mm. The sum of the inlet 1 width $L1$ and inlet 2 width $L2$ is equal to the outlet width, 10 mm.

2.2 Parameter Definitions

(1) The chamber Reynolds number based on the hydraulic diameter of the swirl chamber is defined as:

$$Re_D = \frac{\rho \bar{u}_x D}{\mu} \quad (1)$$

where \bar{u}_x is the mean axial velocity of the swirl chamber and D is the hydraulic diameter of the swirl chamber. μ represents the liquid viscosity.

(2) The swirl number (S) is defined as the ratio of the angular momentum to the axial momentum of the flow as follows(Lin *et al.* 2013):

$$S = \frac{\dot{I}_\phi}{\dot{I}_x} = \frac{2 \int_A \rho u_x u_\phi r dA}{D \int_A \rho u_x u_x dA} \quad (2)$$

where \dot{I}_ϕ is angular momentum with respect to the cylinder axis and \dot{I}_x is axial momentum. R is the tube radius and D is the tube diameter. u_ϕ is the circumferential velocity and u_x is the axial velocity. A is the circular section area, $dA = 2\pi r dr$.

(3) The area average pressure is defined as follows:

$$P = \int_A P_i dA \quad (3)$$

where P_i is the static pressure.

(4) The global average Nusselt number is a measure of the convective heat transfer occurring at the surface. This parameter is expressed as:

$$Nu_g = \frac{qD}{\lambda(T_m - T_w)} \quad (4)$$

where q is the target heat flux, T_m is the inlet total temperature of the fluid, T_w is the temperature of the target, D is the diameter of the swirl chamber, and λ is the thermal conductivity.

(5) The circumferential average Nusselt number is defined as:

$$Nu_c = \frac{q_c D}{\lambda(T_c - T_w)} \quad (5)$$

where q_c is the circumferential average heat flux, T_c is the circumferential average temperature of the fluid, T_w is the temperature of the target, D is the diameter of the swirl chamber, and λ is the thermal conductivity.

(5) The thermal performance factor, η , of a swirl tube is good if the device can reach a significant increase in the heat transfer coefficient with a minimum increase in the friction factor(Tamna *et al.* 2016).

$$\eta = \frac{Nu}{f^{1/3}} \quad (6)$$

where Nu and f are the Nusselt number and friction factor of a dual-inlet swirl tube, respectively.

(6) The friction factor f is a measurement based on pressure loss. The friction factor of the tube can be calculated from

$$f = \frac{\Delta P}{(\rho u^2 / 2)(L / d_H)} \quad (7)$$

where $\Delta P = \frac{(P_1 - P_o)Q_1 + (P_2 - P_o)Q_2}{Q_1 + Q_2}$ is the

equivalent pressure drop across the test section, ρ is the density of the fluid, d_H is the hydraulic diameter of the tube, u is the velocity of the fluid, L is the length of the tube, P_1 is the static pressure of inlet 1, P_2 is the static pressure of inlet 2, P_o is the static pressure of outlet, Q_1 is the volume flow of inlet 1 and Q_2 is the volume flow of inlet 2.

(6) The sum of the inlet area, which is the sum of the areas of inlets 1 and 2, is equal to that of the outlet and remains constant. The heights of the inlets and outlet have the same value. The inlet area ratio, R , is equal to the ratio of the width of inlet 1 to the outlet width. The inlet width ratio of the tube can be calculated from

$$R = \frac{L1}{L0} \quad (8)$$

where $L1$ and $L0$ are the width of inlet 1 and the outlet width, respectively.

(7) The normalized Nusselt number is defined as Nu_g / Nu_0 , where Nu_g is global average Nusselt number in this work and Nu_0 is the Nusselt number in smooth channel. The normalized friction factor is defined as f / f_0 , where f is friction factor in this work and f_0 is the friction factor in smooth channel. The Nusselt number and friction factor obtained from the present smooth channel are compared with the correlations of Dittus-Boelter and Blasius found in the literature for turbulent flow in ducts, respectively(Promvonge *et al.* 2010).

The correlation of Dittus-Boelter is as follows:

$$Nu_0 = 0.023 Re_D^{0.8} Pr^{0.4} \quad (9)$$

The Prandtl number is introduced as the ratio of the diffusivity of momentum to the diffusivity of heat. The correlation of Blasius is as follows:

$$f_0 = 0.316 Re_D^{-0.25} \quad (10)$$

2.3 Simulation Method

The experimental data showed that the shear-stress transport (SST) turbulence model performs reasonably well(Luan *et al.* 2018, Medaouar *et al.* 2019). The SST turbulence model was chosen due to its good capability for predicting the heat transfer performance in swirling flow systems with

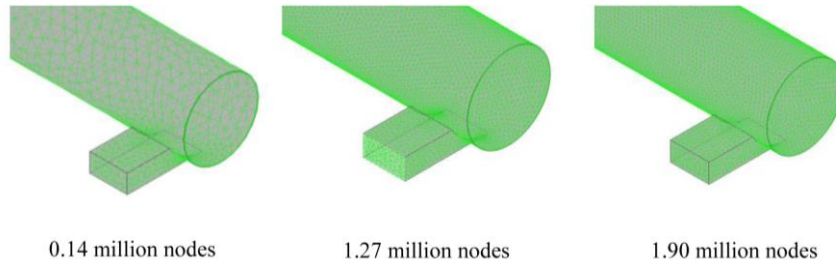


Fig. 3. The mesh of the dual-inlet swirl tube.

comparatively low computational costs.

The continuity equation is:

$$\nabla \cdot (\rho U) = 0 \quad (11)$$

The momentum equation is:

$$\nabla \cdot (\rho U \otimes U) = -\nabla p + \nabla \tau + S_M \quad (12)$$

where τ is the stress tensor and is related to the strain rate by

$$\tau = \mu(\nabla U + (\nabla U)^T) - \frac{2}{3} \delta \nabla U \quad (13)$$

The total energy equation is:

$$\nabla \cdot (\rho U h_{tot}) = \nabla \cdot (\lambda \nabla T) + \nabla \cdot (U \cdot \tau) + U \cdot S_M + S_E \quad (14)$$

where h_{tot} is the total enthalpy, $h_{tot} = h + \frac{1}{2} U^2$,

and S_E is the energy source. The term $\nabla \cdot (U \cdot \tau)$ indicates the work due to viscous stress. In addition, the term $U \cdot S_M$ represents the work due to external momentum sources. Taking the conditions in this study into consideration, $U \cdot S_M$ is neglected in the computation.

Table 1 Boundary conditions for isobaric and isokinetic injection

	Isobaric injection		Isokinetic injection	
Boundary name	Inlet 1	Inlet 2	Inlet 1	Inlet 2
Boundary condition	Velocity inlet	Velocity inlet	Pressure inlet	Pressure inlet
	1.5~7.5 m/s		2300~56000 Pa	

2.4 Simulation Conditions

Steady-state three-dimensional numerical computations were performed. The boundary conditions are shown in Table 1. The swirl tube was heated from the tube wall at a uniform temperature of 473.15 K. The feed fluid was water with a temperature of 298.15 K. All wall surfaces are treated as no-slip boundaries. The computational model includes two adiabatic inlets and one adiabatic outlet.

When the two inlets have equal areas, isokinetic injection and isobaric injection are initialized. For isokinetic injection, the average inlet velocity values are set to 1.5 m/s, 3.0 m/s, 4.5 m/s, 6.0 m/s, and 7.5 m/s, and the corresponding chamber Reynolds numbers are 5352, 10704, 16056, 21408, and 26760, respectively. For isobaric injection, the average inlet pressure values are set to 2300 Pa, 9100 Pa, 20000 Pa, 36000 Pa, and 56000 Pa, and according to a series of exploration simulations, the corresponding chamber Reynolds numbers range from 5357 to 26206.

When the two injection inlets have different areas, the ratio of the area of inlet 1 to the outlet area is set to 0.1, 0.2, 0.5, 0.8, and 0.9, while the sum of the areas of inlets 1 and 2 remains constant and the sum of the inlet areas is equal to that of the outlet. Because the heights of the inlets and outlet have the same value, the area ratio of inlet 1 to inlet 2 is equal to the width ratio of inlet 1 to inlet 2.

2.5 Grid Independence Validation

A proper number of grids guarantees the accuracy of numerical simulations. A careful grid independence check is performed for the computations by considering several grids with nodes ranging from 0.14 million to approximately 1.90 million. For all investigated cases, a tetrahedral mesh is generated using the commercial grid generation software ICEM. The near-wall flow region is meshed with denser grids by using a boundary layer with 3 cell layers, as shown in Fig. 3.

In this paper, we select a case with $Re_D = 16056$ and $R = 0.5$ to validate grid independence. The numbers of mesh nodes in the grid for analysis are 0.14 million, 1.27 million, and 1.90 million. Figure 4 shows the pressure distribution and the circumferentially averaged Nusselt number distribution versus axial length x . This figure shows that the numerical results are not sensitive to the number of grids when the number of grids is greater than 1.27 million. As a result, a grid with 1.27 million nodes is employed.

As denser grids were applied, the computations converged to appropriate values with deviations in the computed fluid outlet temperature and global Nusselt number of less than 1.0%, and these results suggested that the numerical solution is mesh-independent as seen in Table 2. A grid system with approximately 1.27 million nodes was chosen for all computations.

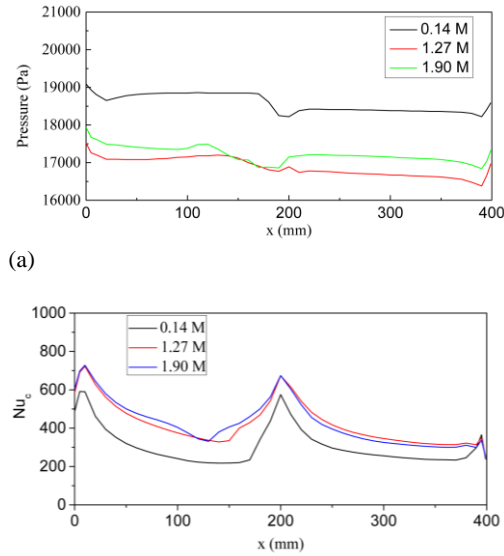


Fig. 4. Grid independence calculation results. (a)The pressure distribution, (b)the circumferential average Nusselt number distribution.

Table 2 Grid independence validation results

	case 1	case 2	case 3
nodes	144998	1268617	1904656
elements	77788	730144	1217830
Nu_g	210	319	317
outlet temperature, K	327.809	343.111	342.865

3. RESULTS AND DISCUSSION

3.1 Comparison Between Isobaric Injection and Isokinetic Injection

The chamber Reynolds number ranges from 5352 to 26760 for isokinetic injection and from 5357 to 26206 for isobaric injection. Therefore, the chamber Reynolds number was kept similar for both feeding modes.

The relationship between the inlet pressures and the chamber Reynolds number is shown in Fig. 5(a) when isokinetic injection is adopted. Both inlet pressures increase rapidly as the chamber Reynolds number rises. Inlet 1 has a higher static pressure than inlet 2. When isokinetic injection is used, the inlet velocity changes along with the chamber Reynolds number, as shown in Fig. 5(b). Both inlet pressures increase proportionally as the chamber Reynolds number rises. Inlet 1 has a lower velocity than inlet 2.

The degree of swirl is usually characterized by the swirl number and, as already mentioned, is defined as the ratio of the angular momentum to the axial momentum of the flow; see Eq. 2. The distributions

of the swirl number along the x axis for isobaric injection and isokinetic injection are shown in Fig. 6. The swirl numbers in all configurations show similar values for each chamber Reynolds number, and most of the swirl numbers range from 0.5 to 2. The highest swirl number appears near inlet 1 for each chamber Reynolds number. First, the swirl number decreases within the tube length after inlet 1. Then, the swirl number increases close to inlet 2, after which the swirl number continues to decrease along the x axis. The swirl number near inlet 2 is less than that near inlet 1. In addition, some fluctuations in the swirl number near inlet 1 for outlet happen due to rapid changes in the velocity direction resulting from the tangential nozzle. The wall friction leads to a similar decreasing circumferential velocity for both isobaric injection and isokinetic injection.

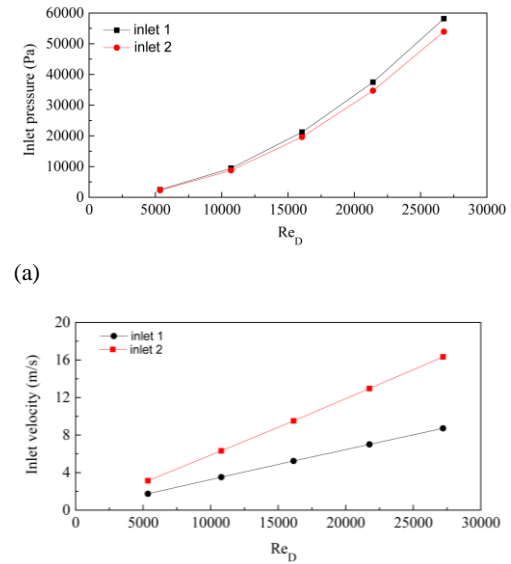


Fig. 5. Changes at inlet versus chamber Reynolds number. (a)for isokinetic injection (b) for isobaric injection is adopted.

The circumferential average Nusselt number distributions along the x axis for isobaric injection and isokinetic injection are shown in Fig. 7. The circumferential average Nusselt number increases as the chamber Reynolds number increases. A higher inlet velocity and higher inlet pressure will lead to a higher circumferential average Nusselt number.

The circumferential average Nusselt numbers show similar changing trends along the x axis. First, the circumferential average Nusselt number decreases within the tube length after inlet 1. Then, the circumferential average Nusselt number increases close to inlet 2, after which the circumferential average Nusselt number continues to decrease along the x axis. The wall friction leads to a similar decreasing circumferential velocity for both isobaric injection and isokinetic injection.

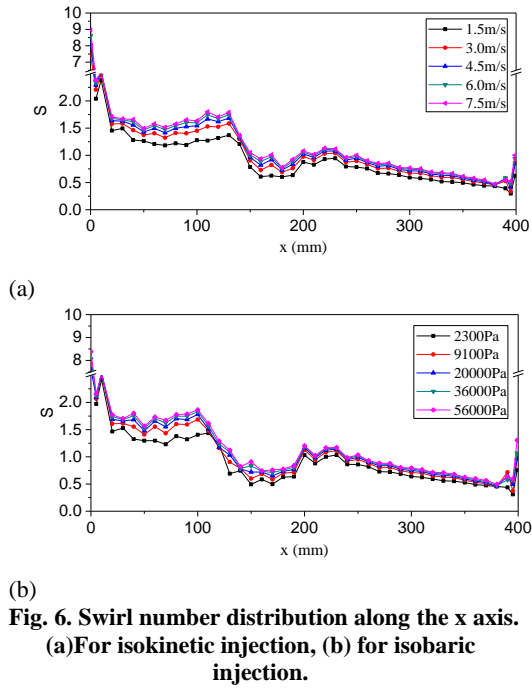


Fig. 6. Swirl number distribution along the x axis. (a)For isokinetic injection, (b) for isobaric injection.

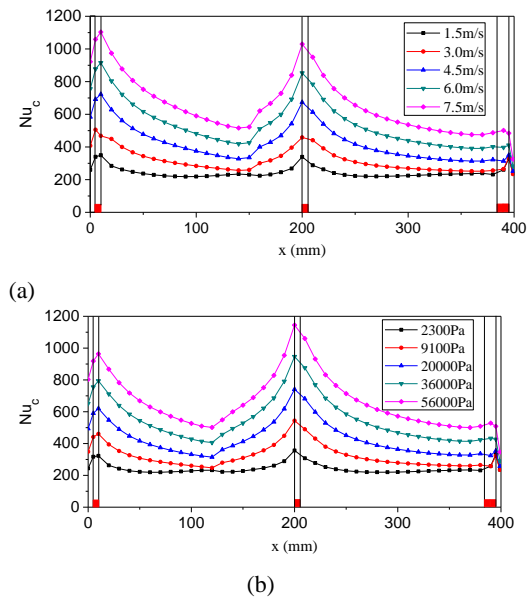


Fig. 7. Circumferential average Nusselt number along the x axis. (a)For isokinetic injection, (b) for isobaric injection.

3.2 The Effect of the Inlet Area Ratio

Isokinetic injection is used when the effect of the inlet area ratio on heat transfer is studied. Because the sum of the inlet areas remains constant, the corresponding chamber Reynolds number also ranges from 5352 to 26760. The inlet area ratios of

the tube are 0.1, 0.2, 0.5, 0.8 and 0.9.

3.2.1 Flow Phenomena

The area pressure at various locations of the swirl tube is recorded from the simulation results. The average inlet velocity values are selected as 1.5 m/s, 4.5 m/s, and 7.5 m/s. The corresponding chamber Reynolds numbers are 5352, 16056, and 26760, respectively. The area average pressure at each location is shown in Fig. 8 when the chamber Reynolds number is 5352, 16056, and 26760, respectively. Inlet 1 has the largest area average pressure, followed by inlet 2 and the outlet in turn. The area average pressure close to inlet 1 exhibits a larger value when R increases.

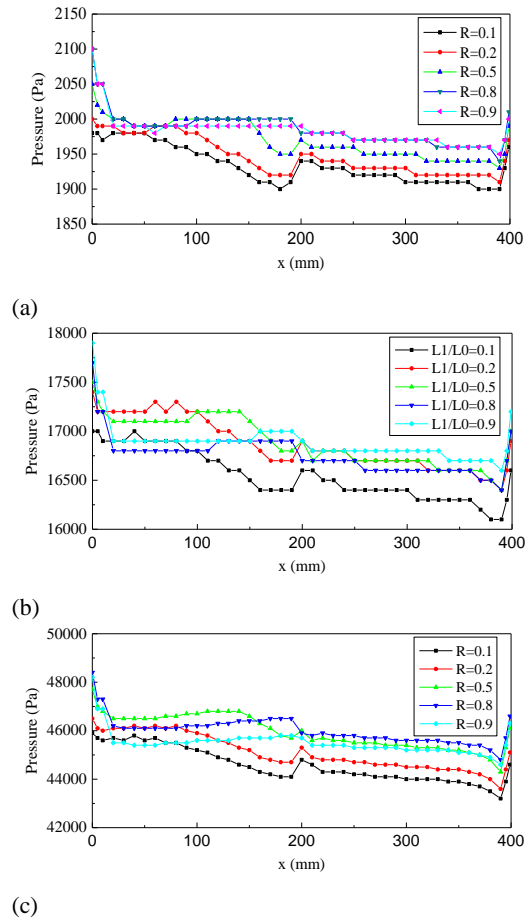


Fig. 8. Area average pressure distribution. (a) the chamber Reynolds number is 5352, (b) the chamber Reynolds number is 16056, (c) the chamber Reynolds number is 26760.

Near the outlet, the area average pressure increases suddenly because of the cyclic dead zone of the streamline. In addition to the position after inlet 2, the area average pressure decreases along the axial direction. The positions between inlet 1 and the outlet exhibit a downward, upward, downward and then upward tendency along the axial direction. For lower values of R , the area average pressure is lower than that for higher values of R in most cases.

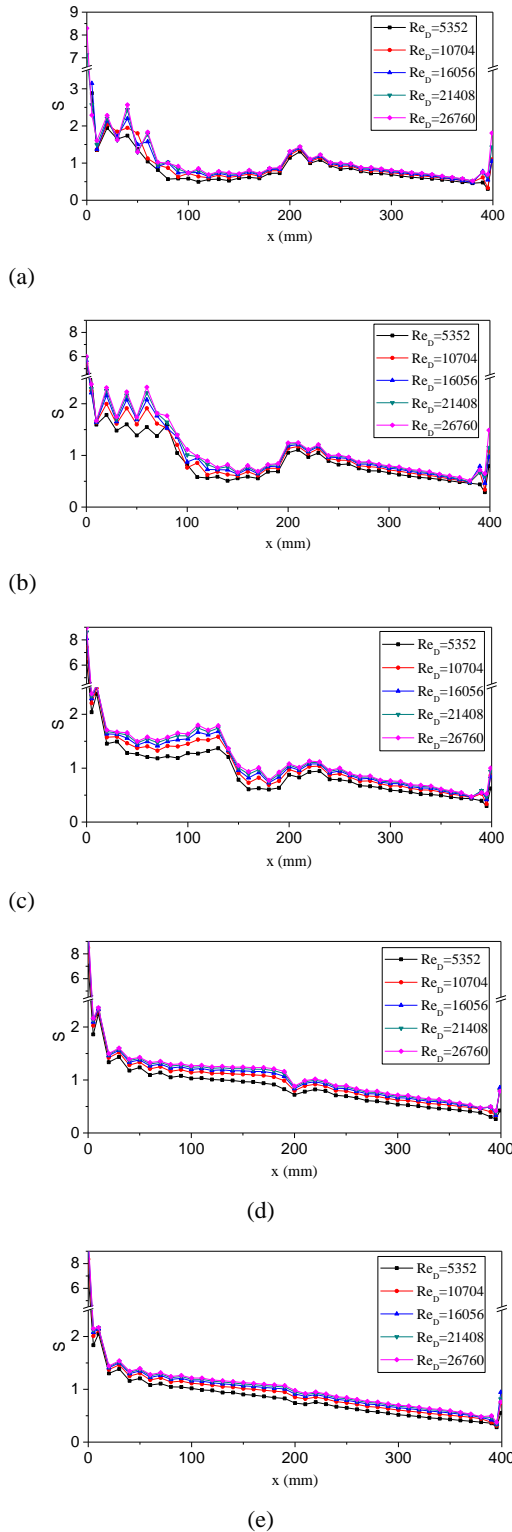


Fig. 9. Swirl number distribution. (a) $R=0.1$, (b) $R=0.2$, (c) $R=0.5$, (d) $R=0.8$, (e) $R=0.9$.

The swirl number in the cross-section area and the continuity equation investigated here are independent of the chamber Reynolds number for each condition of R , as shown in Fig. 9. The swirl numbers vary at different axial positions for all five investigated inlet area ratios. The swirl numbers at inlet 1 have the highest values because the tangential inflow begins to convert to axial velocity.

The swirl number in most cases exhibits a similar range from 0.5 to 2, approximately. However, the swirl number close to inlet 2 has a larger value for a smaller R .

Figure 10 shows the three-dimensional streamline in the swirl chamber when R is 0.8. The color represents the ratio of the liquid local velocity to the inlet velocity, u_{in} .

The water is injected into the swirl chamber and forms a high-velocity swirling flow close to inlets 1 and 2. Because of the viscosity, the liquid velocity decreases gradually as the water flows downstream. As the centrifugal force is not enough after inlet 1, the additional injection through inlet 2 provides a supplement for the swirling flow. The great momentum transport at inlet 2 contributes to an increase in the flow centrifugal force. Therefore, the water in the swirl chamber maintains a suitable swirl number from inlet 1 to the outlet.

The streamline radial contraction is not obvious downstream, as has been reported in the literature (Wu *et al.* 2019). This is a result of the lower momentum loss of a tangential outlet than that of a symmetrical outlet (Liu *et al.* 2019). Moreover, it can be seen that the streamline axial stretch distance from inlet 1 remains almost constant downstream as Re_D increases. This result suggests that the dual-inlet swirl structure may result in stable cross flow, which is beneficial to the uniform heat transfer distribution of the swirl chamber. Generally, the trend of the streamline distribution is roughly similar at various Re_D .

Figure 11 provides the three-dimensional streamline in the swirl chamber when Re_D is 16056. When R has a lower value, most of the fluid passing through inlet 2 tends to move upstream of inlet 2 due to the lower pressure loss facing inlet 1. As R increases, the streamline axial stretch distance lengthens downstream of inlet 1 and shortens downstream of inlet 2. In addition, the streamline radial contraction becomes more obvious close to inlet 1 when R is 0.1. This is a result of low momentum, which is caused by the impacts of little mass flow from inlet 1. When R has a higher value, the streamline axial stretch distance is more uniform, and inlet 2 provides opportune assistance to maintain a suitable tangential velocity.

Figure 12 displays the streamline and velocity contours in the longitudinal section when Re_D is 16056. It is noteworthy that vortex pairs are clearly shown in the images. The number and intensity of vortices at locations between inlets 1 and 2 are obviously affected by R . More vortex pairs appear between inlets 1 and 2 with decreasing R . This effect leads to the turbulent kinetic energy becoming enlarged here. The back-forward streamline is enriched with a small value of R and provides back mixing of fluid that contributes to more heat transfer at locations between inlets 1 and 2. As shown in Fig. 22, when the inlet area ratio increases, the vortex intensity tends to decrease at

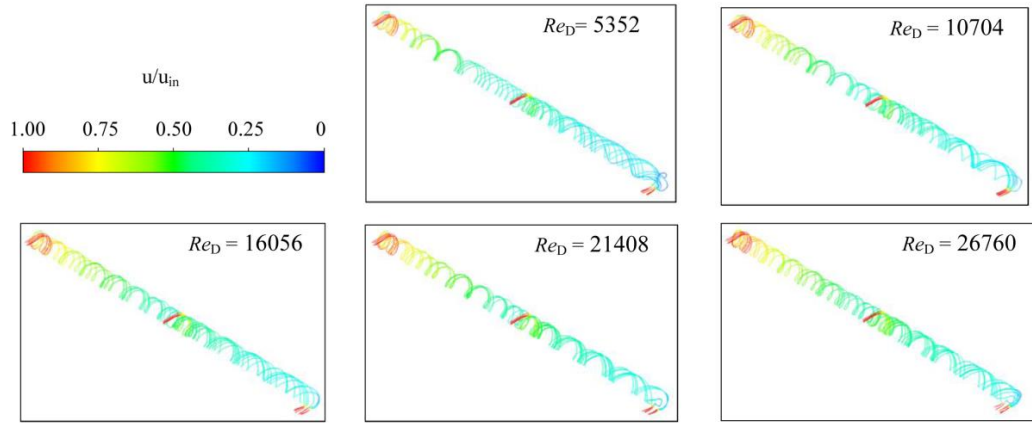


Fig. 10. Three-dimensional streamline in the.

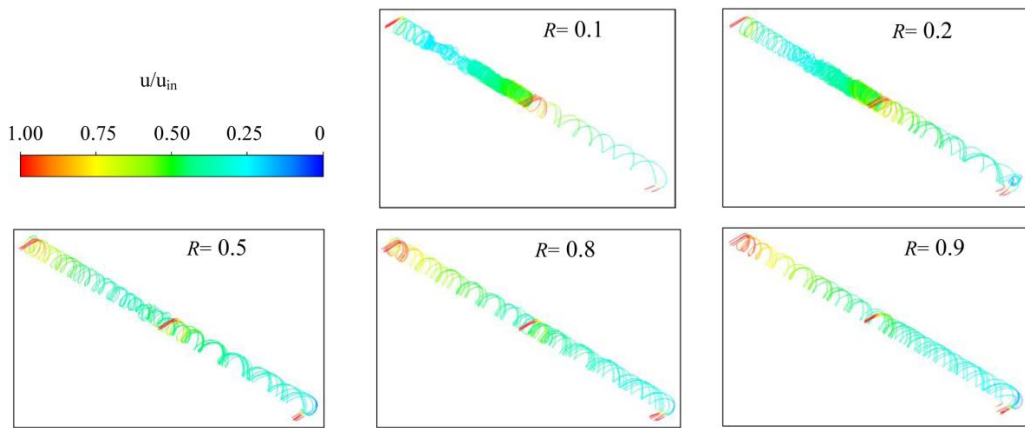


Fig. 11. Three-dimensional streamline in the swirl chamber when Re_D is 16056.

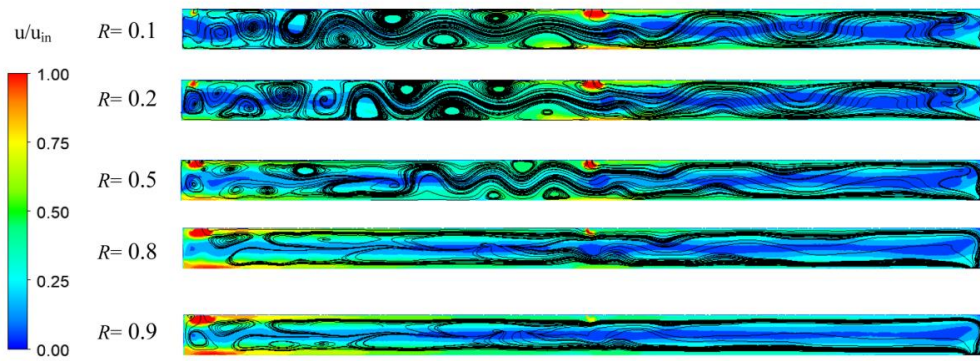


Fig. 12. Streamlines in the longitudinal section for different configurations of R when Re_D is 16056.

locations between inlet 1 and the outlet. Nevertheless, there is a larger velocity upstream of inlet 2 when R is smaller because little mass flow is injected into inlet 1. This tendency relieves as R increases.

3.2.2 Thermal Performance

Figure 13 shows the distributions of Nu contours at different R values when Re_D is 16056. It is clearly

shown that the high heat transfer intensity region corresponds to the inlet location, and the high heat transfer intensity decreases gradually along the axial direction. The lower velocities away from the inlets weaken the impacts of fluid scouring on the target wall boundary layer. As a result, the thickening thermal boundary layer contributes to decreasing the heat transfer intensity.

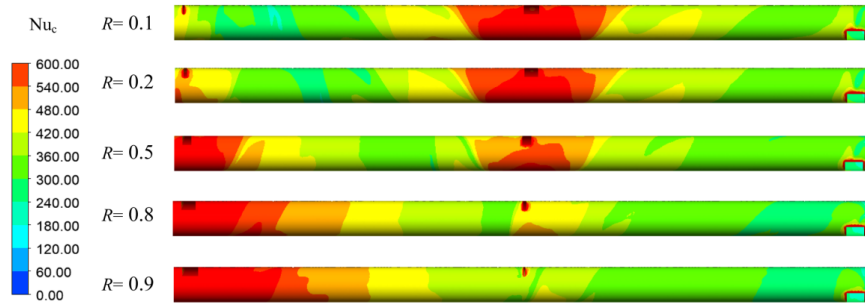


Fig. 13. Contours of the Nusselt number on the target for different configurations of R when Re_D is 16056.

When R has a lower value, the main region for heat transfer is symmetrically distributed on both sides of inlet 2. Part of the fluid passing through inlet 2 flows back toward the upstream and then flows downstream along the x -axis direction. Thus, back mixing happens when R is lower. When R has a higher value, the main region for heat transfer is located downstream of inlet 1.

The variations in the circumferential average Nusselt number in the swirl chamber along the axial direction for different R values are shown in Figs. 14~18. For each figure, five kinds of inlet velocities are used to obtain the relationship between the inlet velocity and the circumferential average Nusselt number. Inlets 1 and 2 exhibit peak values of the circumferential average Nusselt number. This is because the tangential velocity of the water increases and vortices appear, which contribute to high turbulence and mixing. The circumferential average Nusselt number increases when the water flow has a high tangential velocity ejected from the inlets. The injected water not only violently washes the wall of the swirl chamber, reducing the thickness of the thermal boundary layer, but also generates vortices that enhance the turbulence and mixing. As the inlet area ratio increases, the circumferential average Nusselt number at inlet 1 rises, and the circumferential average Nusselt number at inlet 2 decreases. The mass flow dominates the circumferential average Nusselt number near the inlets.

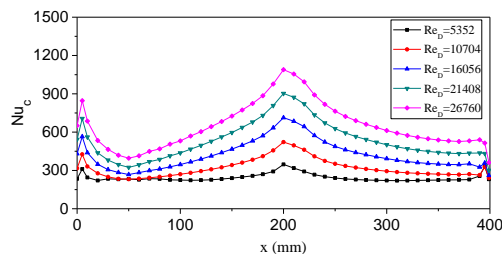


Fig. 14. Circumferential average Nusselt number along the axial direction for different chamber Reynolds numbers when R is 0.1.

The global average Nusselt number distributions for different structures and chamber Reynolds numbers are shown in Fig. 19. The global average Nusselt

number increases with increasing chamber Reynolds number. For a certain chamber Reynolds number, different values of R lead to variations in the global average Nusselt number, as shown in each line in Fig. 19. In most cases, the global average Nusselt number increases with R and then decreases with R . An R value of 0.5 exhibits the largest global average Nusselt number for each chamber Reynolds number.

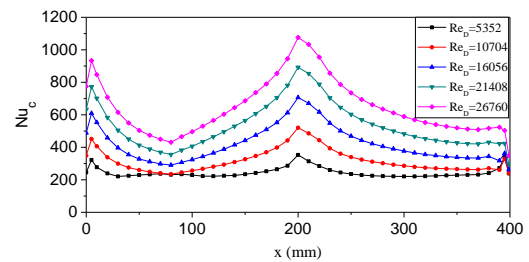


Fig. 15. Circumferential average Nusselt number along the axial direction for different chamber Reynolds numbers when R is 0.2.

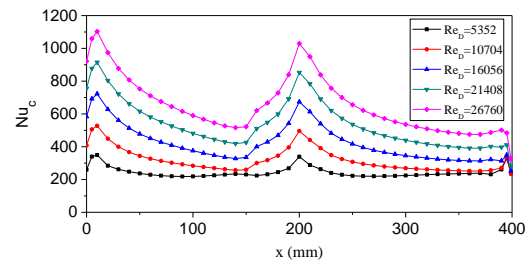


Fig. 16. Circumferential average Nusselt number along the axial direction for different chamber Reynolds numbers when R is 0.5.

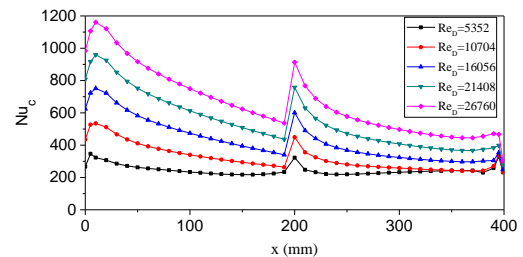


Fig. 17. Circumferential average Nusselt number along the axial direction for different chamber Reynolds numbers when R is 0.8.

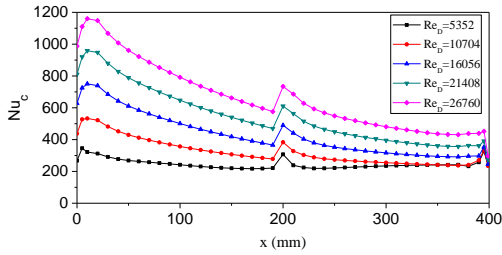


Fig. 18. Circumferential average Nusselt number along the axial direction for different chamber Reynolds numbers when R is 0.9.

According to the changes in the normalized Nusselt number with R shown in Fig. 20, an R value of 0.5 exhibits the peak value of the normalized Nusselt number for each chamber Reynolds number. This result means that an equal area distribution of the inlets is advantageous over the other configurations.

The dual-inlet swirl tube yields considerable heat transfer compared with the plain tube. According to the values of normalized Nusselt number (Nu_g / Nu_0), the global average Nusselt number of the tube insert (Nu_g) is much higher than that of the plain tube (Nu_0). This result is due to stronger vortex strength helping to increase the turbulence intensity and a thinner boundary layer, resulting in higher convection. For chamber Reynolds numbers ranging from 10704 to 26760, the normalized Nusselt number with an R value of 0.1 is lower than that with an R value of 0.9, and the normalized Nusselt number with an R value of 0.2 is lower than that with an R value of 0.8. For a chamber Reynolds number of 5352, the normalized Nusselt number with an R value of 0.1 is higher than that with an R value of 0.9, and the normalized Nusselt number with an R value of 0.2 is higher than that with an R value of 0.8.

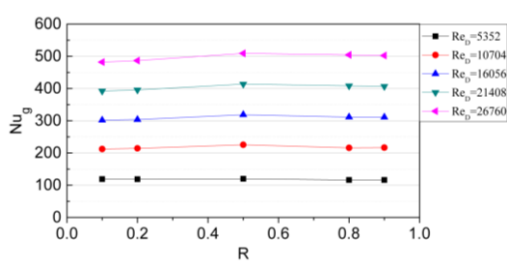


Fig. 19. Changes in the global average Nusselt number with R for different chamber Reynolds numbers.

The influences of using the dual-inlet swirl tube on the friction factors and normalized friction factors are displayed in Figs. 31 and 32, respectively. These figures show that the application of the swirl tube leads to a substantial increase in the friction factor above that of the plain tube.

As shown in Fig. 21, the friction factor shows a

downtrend and uptrend with increasing R for Re_D values of 5352, 10704, 16056, 21408, and 26760. As shown in Fig. 22, the normalized friction factor increases with increasing chamber Reynolds number, with the exception of cases in which R is equal to 0.1. This has some difference from the ideal fact that the friction factor will increase with the R value. This may result from the fact that the large resistance of tangential inlet 1 due to small equivalent diameter of inlet 1 when R is equal to 0.1 or 0.2. The normalized friction factor exhibits a greater value for higher values of Re_D .

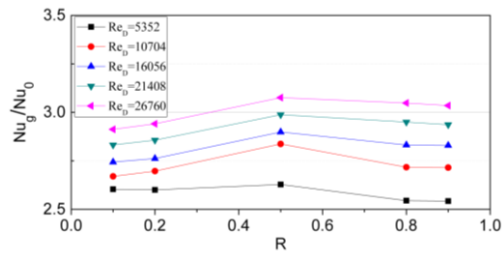


Fig. 20. Changes in the normalized Nusselt number with R for different chamber Reynolds numbers.

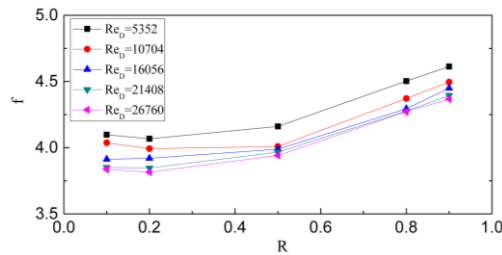


Fig. 21. Changes in the friction factor with R for different chamber Reynolds numbers.

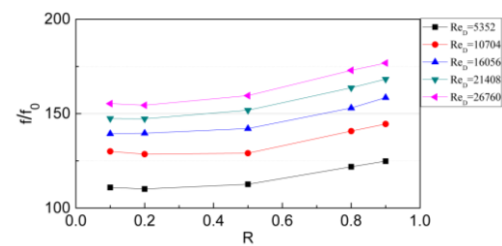


Fig. 22. Changes in the normalized friction factor with R for different chamber Reynolds numbers.

Figure 23 portrays the effect of the inlet area ratio, R , on the thermal performance factor, η . For chamber Reynolds numbers of 10704, 16056, 21408, and 26760, the thermal performance factor shows an uptrend and downtrend with increasing R from 0.1 to 0.9. According to flow phenomena and heat transfer characteristics, more fluid through inlet 1 will result in higher temperature at outlet and higher pressure loss. More fluid through inlet 2 will result in lower temperature at outlet and lower

pressure loss. The maximum value of the thermal performance factor happens with an R value of 0.5. The structure parameter, R , should be selected as 0.5 as far as possible to obtain more heat transfer with a lower pressure loss. The correlation curve between thermal performance factor and inlet area ratio shows symmetry basically around $R=0.5$ for chamber Reynolds numbers ranging from 10704 to 26760. The minimum value of the thermal performance factor happens with R values of 0.1 and 0.9 which should be avoided for industrial application. For chamber Reynolds numbers of 5352, the thermal performance factor shows a downtrend with increasing R from 0.1 to 0.9.

What should be noticed that the thermal performance factor exhibits within the range from 0.510 to 0.570 for all cases. When Re_D is equal to 26760 exhibits a maximum of the thermal performance factor for all the values of R . To guide economic designs of heat exchangers, an inlet area ratio value of 0.5 is preferred. The heated water temperatures at outlet are shown in Table 3. The water is preheated from 25 °C to 70 °C approximately which would be benefit to the degassing of acidic water.

Table 3 Water temperatures at outlet with an inlet area ratio value of 0.5

Chamber Reynolds number	water temperatures at outlet (K)	thermal performance factor
5352	348.93	0.544
10704	345.87	0.561
16056	343.11	0.555
21408	341.91	0.560
26760	341.23	0.567

When the swirl tube is used to preheating water, the handling capacity is controlled with chamber Reynolds number closed to 26760. The thermal performance factor shows similar trend basically with chamber Reynolds numbers of 10704, 16056, 21408, and 26760 which indicates that the heat transfer performance keeps stable within this range of handling capacity.

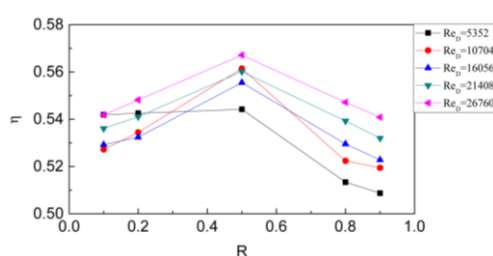


Fig. 23. Variation in η with R for the dual-inlet swirl tube.

4. CONCLUSION

In this paper, numerical simulations are performed to investigate dual-inlet swirl heating characteristics. Detailed grid independence analysis validation is conducted to acquire proper calculation results. The influences of the feeding mode and inlet area ratio are investigated for further study of the details of swirl heating.

When isokinetic injection is used, inlet 1 has a lower velocity than inlet 2. The circumferential average Nusselt number near inlet 2 is similar to that near inlet 1 for isokinetic injection, while the circumferential average Nusselt number near inlet 2 is higher than that near inlet 1 for isobaric injection. The inlet velocity dominates the local Nusselt number.

The inlet area ratio R has a remarkable influence on the flow and heat transfer behavior of swirl heating. When the chamber Reynolds number is kept unchanged, the swirl number close to inlet 2 has a larger value for a smaller R . A lower value of R leads to the tendency for the fluid passing through inlet 2 to move upstream of inlet 2 and results in more vortex pairs between inlets 1 and 2. The back-forward streamline is enriched with a small value of R and provides back mixing of fluid that contributes to more heat transfer.

Larger chamber Reynolds number will lead to larger global average Nusselt number. An R value of 0.5 exhibits the largest global average Nusselt number and the peak value of the normalized Nusselt number for each chamber Reynolds number. Additional fluid through inlet 2 provides an opportune assistance to maintain a more uniform swirl number for a value of 0.5. For the Re_D values ranging from 5352 to 26760, the inlet area ratio, R , should be kept as 0.5 as far as possible to obtain more heat transfer with a low pressure loss. Inlet area ratio values of 0.1 and 0.9 will lead to bad thermal performance which should be avoided.

Preheating exchanger is widely used in petroleum, chemical industry, electric power, metallurgy, shipbuilding and other industrial fields. It is not only essential equipment in industrial production but also one of the main equipment to improve energy efficiency. Moreover, deep-sea probes, offshore drilling platforms and space vehicles are in harsh environments (high-pressure difference and high-temperature differences), which demand higher requirements on the volume, weight, strength and heat transfer performance of the preheating exchanger. In recent years, the preheating exchanger industry has also shown a trend of miniaturization, high efficiency and energy saving in terms of products and technologies. The preheating exchanger has a great impact on the national economy, so it has a bright future.

ACKNOWLEDGMENTS

The authors wish to express their sincere gratitude

to the National Key R&D Program of China (2018YFC1802704, 2018YFC1801904), National Natural Science Foundation of China (51678238, 51722806, 51608325, 21908057), China Postdoctoral Science Foundation funded project (2018M641942), and Shanghai Sailing Program (19YF1411800) for financial support.

REFERENCES

- Awais, M. and A. A. Bhuiyan (2018). Heat transfer enhancement using different types of vortex generators (VGs): A review on experimental and numerical activities. *Thermal Science and Engineering Progress* 5, 524-545.
- Biegger, C., Y. Rao and B. Weigand (2018). Flow and heat transfer measurements in swirl tubes with one and multiple tangential inlet jets for internal gas turbine blade cooling. *International Journal of Heat and Fluid Flow* 73, 174-187.
- Chen, B., K. Ho, Y. A. Abakr and A. Chan (2016b). Fluid dynamics and heat transfer investigations of swirling decaying flow in an annular pipe Part 2: Fluid flow. *International Journal of Heat and Mass Transfer* 97, 1012-1028.
- Chen, B., K. Ho, Y. A. Abakr and A. Chan (2016a). Fluid dynamics and heat transfer investigations of swirling decaying flow in an annular pipe Part 1: Review, problem description, verification and validation. *International Journal of Heat and Mass Transfer* 97, 1029-1043.
- Chen, X., T. Zhao, M. Q. Zhang and Q. Chen (2019). Entropy and entransy in convective heat transfer optimization: A review and perspective. *International Journal of Heat and Mass Transfer* 137, 1191-1220.
- Hong, Y., J. Du, S. Wang, S. M. Huang and W. B. Ye (2018). Effect of decaying swirl flow on tubular turbulent heat transfer enhancement by using short length helical tapes. *Chemical Engineering Research and Design* 138, 1-12.
- Jafari, M., S. Dabiri, M. Farhadi and K. Sedighi (2017). Effects of a three-lobe swirl generator on the thermal and flow fields in a heat exchanging tube: An experimental and numerical approach. *Energy Conversion and Management* 148, 1358-1371.
- Khaleghinia, J., F. Kowsary and C. Aghanajafi (2019). Optimization of Synthetic Jet Position for Heat Transfer Enhancement and Temperature Uniformity of a Heated Wall in Micro-Channels. *Journal of Applied Fluid Mechanics* 12(5), 1429-1437.
- Kreith, F. and D. Margolis (1959). Heat Transfer and Friction in Turbulent Vortex Flow. *Applied Sci. Research* 8, 457-473.
- Lin, G., K. Kusterer, D. Bohn, T. Sugimoto, R. Tanaka and M. Kazari (2013). Investigation on heat transfer enhancement and pressure loss of double swirl chambers cooling. *Propulsion and Power Research* 2(3), 177-187.
- Ling, J. P. C. W., P. T. Ireland and N. W. Harvey (2006, May). Measurement of Heat Transfer Coefficient Distributions and Flow Field in a Model of a Turbine Blade Cooling Passage with Tangential Injection. In *Proceedings of ASME Turbo Expo 2006: Power for Land, Sea, and Air*, Barcelona, Spain
- Liu, Y., Y. Rao and B. Weigand (2019) Heat transfer and pressure loss characteristics in a swirl cooling tube with dimples on the tube inner surface. *International Journal of Heat and Mass Transfer* 128, 54-65.
- Luan, Y., C. Du, X. Fan, J. Wang and L. Li (2018). Investigations of flow structures and heat transfer in a swirl chamber with different inlet chambers and various aerodynamic parameters. *International Journal of Heat and Mass Transfer* 118, 551-561.
- Medaouar, W., L. Loukarfi, M. Braikia, A. Khelil and H. Naji (2019). Experimental and Numerical Study of a Turbulent Multiple Jets Issued from Lobed Diffusers. *Journal of Applied Fluid Mechanics* 12(3), 729-742.
- Mothilal, T., K. Pitchandi, V. Velukumar and K. Parthiban (2018). CFD and Statistical Approach for Optimization of Operating Parameters in a Tangential Cyclone Heat Exchanger. *Journal of Applied Fluid Mechanics* 11(2), 459-466.
- Promvong, P., T. Chompookham, S. Kwankaomeng and C. Thianpong (2010). Enhanced heat transfer in a triangular ribbed channel with longitudinal vortex generators. *Energy Conversion and Management* 51(6), 1242-1249.
- Sheikholeslami, M., M. Gorji-Bandpy and D. D. Ganji (2015). Review of heat transfer enhancement methods: Focus on passive methods using swirl flow devices. *Renewable and Sustainable Energy Reviews* 49, 444-469.
- Tamna, S., Y. Kaewkohkiat, S. Skullong and P. Promvong (2016). Heat transfer enhancement in tubular heat exchanger with double V-ribbed twisted-tapes. *Case Studies in Thermal Engineering* 7, 14-24.
- Vahidifar, S. and M. Kahrom (2015). Experimental Study of Heat Transfer Enhancement in a Heated Tube Caused by Wire-Coil and Rings. *Journal of Applied Fluid Mechanics* 8(4), 885-892.
- Wu, F., L. Li, C. Du, J. Wang and X. Fan (2019). Effects of circumferential nozzle number and temperature ratio on swirl cooling characteristics. *Applied Thermal Engineering* 154, 332-342.
- Xu, X., H. Lu, Y. Qian, B. Zhang, H. Wang, H. Liu and Q. Yang (2019). Gas-liquid mass transfer and bubble size distribution in a multi-Cyclone

- separator. *AIChE Journal* 65(1), 221-229.
- Xu, X., Q. Yang, C. Wang and H. Wang (2015). Impact of bubble coalescence on separation performance of a degassing hydrocyclone. *Separation and Purification Technology* 152, 80-86.
- Xu, X., Q. Yang, C. Wang, X. Ge and H. Wang (2016). Dissolved gas separation using the pressure drop and centrifugal characteristics of an inner cone hydrocyclone. *Separation and Purification Technology* 161, 121-128.
- Xu, X., X. Ge, Y. Qian, H. Wang and Q. Yang (2018). Bubble-separation dynamics in a planar cyclone: Experiments and CFD simulations. *AIChE Journal* 64(7), 2689-2701.